The Supersonic Project: Lighting Up the Faint End of the JWST UV Luminosity Function

Claire E. Williams[1,2], William Lake[1,2], Smadar Naoz[1,2], Blakesley Burkhart[3,4], Tommaso Treu[1],
Federico Marinacci[5], Yurina Nakazato[6], Mark Vogelsberger[7], Naoki Yoshida[6,8,9], Gen Chiaki[10],
Yeou S. Chiou[1,2], and Avi Chen[3]

[1] Department of Physics and Astronomy, UCLA, Los Angeles, CA 90095, USA; clairewilliams@astro.ucla.edu
[2] Mani L. Bhaumik Institute for Theoretical Physics, Department of Physics and Astronomy, UCLA, Los Angeles, CA 90095, USA
[3] Department of Physics and Astronomy, Rutgers, The State University of New Jersey, 136 Frelinghuysen Road, Piscataway, NJ 08854, USA
[4] Center for Computational Astrophysics, Flatiron Institute, 162 Fifth Avenue, New York, NY 10010, USA
[5] Department of Physics & Astronomy "Augusto Righi," University of Bologna, via Gobetti 93/2, I-40129 Bologna, Italy
[6] Department of Physics, The University of Tokyo, 7-3-1 Hongo, Bunkyo, Tokyo 113-0033, Japan
[7] Department of Physics and Kavli Institute for Astrophysics and Space Research, Massachusetts Institute of Technology, Cambridge, MA 02139, USA
[8] Kavli Institute for the Physics and Mathematics of the Universe (WPI), UT Institute for Advanced Study, The University of Tokyo, Kashiwa, Chiba 277-8583, Japan
[9] Research Center for the Early Universe, School of Science, The University of Tokyo, 7-3-1 Hongo, Bunkyo, Tokyo 113-0033, Japan
[10] Astronomical Institute, Tohoku University, 6-3, Aramaki, Aoba-ku, Sendai, Miyagi 980-8578, Japan

Abstract

The James Webb Space Telescope (JWST) is capable of probing extremely early eras of our Universe, when the supersonic relative motions between dark matter and baryonic overdensities modulate structure formation ($z \gtrsim 10$). We study low-mass galaxy formation, including this "stream velocity," using high-resolution AREPO hydrodynamics simulations and present theoretical predictions of the UV luminosity function (UVLF) and galaxy stellar mass function down to extremely faint and low-mass galaxies ($M_{UV} \gtrsim -15$, $10^4 M_\odot \leqslant M_* \leqslant 10^8 M_\odot$). We show that, although the stream velocity suppresses early star formation overall, it induces a short period of rapid star formation in some larger dwarfs, leading to an enhancement in the faint end of the UVLF at $z = 12$. We demonstrate that JWST observations are close to this enhanced regime and propose that the UVLF may constitute an important probe of the stream velocity at high redshift for JWST and future observatories.

1. Introduction

The James Webb Space Telescope (JWST) has opened a new window on the first galaxies in the Universe, allowing for new insights regarding their properties and formation. These galaxies at "cosmic dawn" host the yet-undetected first generation of stars (Population III), reionize the Universe, and enrich their surroundings with the first metals. The ΛCDM (cold dark matter + cosmological constant) cosmological model predicts the formation of these early sources within the first few hundred million yr after the Big Bang (e.g., Vogelsberger et al. 2020a). Observations of faint galaxies at high redshift represent an opportunity to test galaxy formation models and the ΛCDM paradigm itself.

Since JWST began science operations in 2022, NIRCam data sets have provided a number of intriguing galaxy candidates at $z > 9$ (e.g., Bradley et al. 2023; Castellano et al. 2022, 2023; Finkelstein et al. 2022; Naidu et al. 2022; Adams et al. 2023; Atek et al. 2023; Bouwens et al. 2023; Donnan et al. 2023a, 2023b; Morishita & Stiavelli 2023; Pérez-González et al. 2023; Yan et al. 2023). Furthermore, JWST's spectrographic instruments allow for precision redshift determination, and multiple galaxies with $z > 9$ have been confirmed, with gravitationally lensed systems providing an additional magnified glimpse at the early Arrabal Haro et al. 2023; Atek et al. 2023; Williams et al. 2023; Universe (e.g., Roberts-Borsani et al. 2023).

Moreover, robust measurements of the UV luminosity function (UVLF) are now possible down to very faint magnitudes (e.g., Naidu et al. 2022; Castellano et al. 2023; Donnan et al. 2023a; Finkelstein et al. 2023; Harikane et al. 2023, 2024; Leung et al. 2023) at redshifts $z \sim 12$ and beyond. These observations open a window into the physics of galaxy formation at increasingly small scales and high redshifts.

Low-mass (baryonic mass $M_b \lesssim 10^9 M_\odot$) galaxies represent a sensitive test of galaxy formation and cosmological models due to their small gravitational potentials, which are sensitive to the precise nature of dark matter (DM) and baryonic physics (e.g., Bullock & Boylan-Kolchin 2017; Sales et al. 2022). In order to compare the wealth of JWST data to cosmological models, a precise description of the baryonic physics that dictates the formation of these dwarf galaxies is necessary (e.g., Shen et al. 2020, 2023; Vogelsberger et al. 2020b). Within the standard ΛCDM model, these galaxies originate from small-scale ($k \gtrsim 20\,\mathrm{Mpc}^{-1}$) baryonic density fluctuations whose growth is dictated by the overwhelming gravitational potential of DM overdensities. The latter is orders of magnitude larger than the baryonic overdensities by the time of recombination (e.g., Naoz & Barkana 2005; Loeb & Furlanetto 2013).

Tseliakhovich & Hirata (2010) showed that a second-order term in standard linear perturbation theory, the relative velocity between DM and baryons (v_{bc}), is nonnegligible at these scales, with an rms value (σ_{vbc}) at $z = 1100$ of $30\,\mathrm{km\,s^{-1}}$, five times the speed of sound at that time. This stream velocity was shown to delay the formation of Population III stars, suppress halo abundance, and raise the minimum halo mass that can retain

baryons and form stars (e.g., Greif et al. 2011; Stacy et al. 2011; Bovy & Dvorkin 2013; Naoz et al. 2013; Asaba et al. 2016; Schauer et al. 2017a, 2021, 2023; Conaboy et al. 2023; Hegde & Furlanetto 2023; Nebrin et al. 2023). Notably, the stream velocity was recently estimated locally to be $v_{bc} = 1.75^{+0.13}_{-0.28}\sigma_{vbc}$ (Uysal & Hartwig 2023).

This supersonic velocity generates a phase shift between the baryonic and DM perturbations that introduces a physical offset between the center of mass of collapsed baryon structures and their parent DM halo (e.g., Naoz & Narayan 2014; Popa et al. 2016; Chiou et al. 2018, 2019, 2021; Lake et al. 2021, 2023a, 2023b; Nakazato et al. 2022; Williams et al. 2023). The physical offset between the DM and baryonic components of ΛCDM overdensities and other effects of the stream velocity have important implications for the formation of the first stars and galaxies, with potential consequences for JWST observations. In some cases, for very low mass halos ($M_b \lesssim 10^5 M_\odot$), the physical offset is so large that baryons collapse outside of their parent DM halo, creating DM-free supersonically induced gas objects (SIGOs), which may be the progenitors of some early globular clusters (e.g., Popa et al. 2016; Chiou et al. 2018, 2019, 2021; Lake et al. 2021, 2023a; Nakazato et al. 2022). Future JWST observations may reveal a population of star clusters at high galactocentric distances descended from SIGOs at high redshift (Lake et al. 2023b). For halos with $M_b \lesssim 10^9 M_\odot$, the physical offset results in the formation of diffuse structures called Dark Matter + Gas Halos Offset by Streaming (DM GHOSts; e.g., Williams et al. 2023). Unlike typical dwarf galaxies, these structures are highly elongated, more rotationally supported, and gas-deficient, as the stream velocity advects a portion of the gas component out of the halo (e.g., Hirano et al. 2023; Williams et al. 2023).

The delay of star formation and the diffuse nature of the structures that form in regions of streaming have implications for the populations of dwarf galaxies that exist in the high-redshift Universe. Here, we suggest that the stream velocity may affect the faint end of the UVLF by suppressing star formation in the smallest galaxies and boosting the star formation rate (SFR) of larger dwarfs for a short period around $z \sim 12$. We estimate the galaxy stellar mass function (GSMF), showing that the stream velocity suppresses the low-mass end. We suggest that JWST and future extremely large telescopes have the opportunity to observe galaxies at extremely high redshift in regions of supersonic streaming. These results imply that the stream velocity will enhance the scatter in the UVLF at faint M_{UV}.

The structure of this paper is as follows. In Section 2, we describe the AREPO simulations used and their initial conditions, including the stream velocity. In Section 3, we describe the GSMF (Section 3.2) and UVLF (Section 3.3) at high redshifts in regions of the Universe with and without streaming. Finally, in Section 4, we interpret these results and the outlook for JWST observations.

In this study, we assume a ΛCDM cosmology, with $\Omega_\Lambda = 0.73$, $\Omega_m = 0.27$, $\Omega_b = 0.044$, $\sigma_8 = 1.7$, and $h = 0.71$. Magnitudes are calculated using the AB magnitude system; $m = -2.5\log_{10}(f_\nu/\text{nJy}) + 31.40$ (Oke 1974).

2. Methods

2.1. Cosmological Simulation Description

We perform a suite of numerical simulations in AREPO (Springel 2010), evolving a box $(2.5\ h^{-1}\ \text{Mpc})^3$ from $z = 200$

to 12. To generate initial conditions, we use a modified CMBFAST code (Seljak & Zaldarriaga 1996). As in Popa et al. (2016), we include the first-order correction of scale-dependent temperature fluctuations on the initial conditions and their transfer functions as in Naoz & Barkana (2005) and Naoz & Narayan (2013). This allows for accurate gas fractions in halos at high redshift (e.g., Naoz et al. 2009, 2011, 2013). The box contains 768^3 DM particles ($m_{DM} = 775\ h^{-1} M_\odot$) and 768^3 Voronoi mesh gas cells, giving a gas cell resolution of $m_{gas} = 200\ M_\odot$. See Lake et al. (2023b) for the simulation suite details.

On scales smaller than a few Mpc, the relative velocity is coherent and can be modeled as a bulk stream motion (e.g., Tseliakhovich & Hirata 2010; Popa et al. 2016) with an rms value of σ_{bc}. We initialize our simulations at $z = 200$, when a $2\sigma_{bc}$ fluctuation in the stream velocity corresponds to 11.8 km s^{-1} (e.g., Popa et al. 2016). The stream velocity is thus implemented as a uniform boost of 11.8 (km s^{-1})$\hat{x}$ to all baryon particles. In order to compare the properties of early galaxies in regions with and without a highly supersonic stream velocity, we perform two simulation runs, one with a $0\sigma_{bc}$ fluctuation (i.e., no stream velocity) and one with a $2\sigma_{bc}$ fluctuation (a value similar to the observed local one; Uysal & Hartwig 2023).

In order to increase the statistical power of our simulation without affecting the underlying cosmology, we choose $\sigma_8 = 1.7$ (these are the same simulations as in Lake et al. 2023b). Thus, our box represents a strong density peak where structure in the Universe forms early, such as in the Virgo cluster (e.g., Naoz & Barkana 2007). These results and their robust statistics can thus be scaled to other regions of the Universe accordingly (e.g., Naoz & Narayan 2013; Park et al. 2020; see Appendix A).

2.2. Subgrid Physics: Cooling and Star Formation

An accurate prescription of molecular cooling in the pristine gas of the early Universe is necessary to model the formation and collapse of gas-rich structures at high redshift (e.g., Schauer et al. 2021; Nakazato et al. 2022; Lake et al. 2023a; Williams et al. 2023). Following Nakazato et al. (2022), Lake et al. (2023a), and Williams et al. (2023), we include molecular cooling in both runs through the GRACKLE chemistry and cooling library (Smith et al. 2017; Chiaki & Wise 2019). This prescription explicitly accounts for nonequilibrium chemical reactions and radiative cooling, including 15 primordial species (e^-, H, H$^+$, He, He$^+$, He^{++}, H$^-$, H$_2$, H$_2^+$, D, D$^+$, HD, HeH$^+$, D$^-$, and HD$^+$).

Once the gas condenses sufficiently, the first generation of stars forms. As described in Lake et al. (2023b), when a gas cell exceeds the Jeans mass, it collapses to form a star particle on the freefall timescale. The SFR for a given object is computed as the difference in its stellar mass between two snapshots, excluding any star particles that were part of a cluster that merged into the halo. We do not include any stellar feedback effects, although feedback processes are vital to understand the efficiency of star formation over cosmic time to the present day. The resulting estimates of the UVLF can thus be considered an upper limit, given that feedback effects will suppress the efficiency of star formation.

2.3. Identification of Structures

Using a friends-of-friends (FOF) algorithm, we search for two object classes. First, we identify DM-primary/gas-secondary objects, corresponding to DM GHOSts. In this case, the FOF algorithm is run on DM particles first, with gas cells and star particles linked at a secondary stage. We also identify gas-primary objects by running the FOF algorithm on gas cells only. This allows us to find gas clumps without an associated DM halo (SIGOs; see, e.g., Chiou et al. 2018, 2019, 2021; Lake et al. 2021, 2023a, 2023b; Nakazato et al. 2022). In order to avoid nonphysical numerical effects, we require DM-primary objects to contain at least 300 particles and gas-primary objects to have at least 100 cells (e.g., Naoz et al. 2011).

2.4. The UV Luminosity

The rest-frame UV 1500 Å luminosity of high-redshift galaxies observed in the infrared by JWST traces the SFR, assuming that they are dominated by young, massive stars with short lifetimes (e.g., Kennicutt 1998; Stark et al. 2009; Kennicutt & Evans 2012). We calculate the SFR of each object in the simulation by identifying objects in snapshots at $z = 13$ and 12 and calculating the difference in stellar mass between the two snapshots. Given the SFR of galaxies in our simulations at $z = 12$, we then estimate their rest-frame UV continuum luminosity ($L_{\rm UV,1500}$),

$$L_{\rm UV,1500} = \frac{\dot{M}_*}{\mathcal{K}_{\rm UV,1500}}, \qquad (1)$$

where $\dot{M}_*$ is the SFR in units of $M_\odot\,{\rm yr}^{-1}$. $\mathcal{K}_{\rm UV,1500}$ is a fiducial constant evaluated for continuous-mode star formation with a Salpeter initial mass function (IMF). We adopt $\mathcal{K}_{\rm UV,1500} = 1.15 \times 10^{-28}\ M_\odot\,{\rm yr}^{-1}/({\rm erg\ s}^{-1}\,{\rm Hz}^{-1})$ (following, e.g., Madau & Dickinson 2014; Sun & Furlanetto 2016).

This seems to be a reasonable assumption given that we trace the star formation on a timescale of $\sim$30 Myr, which is comparable to the lifetime of the most massive stars. $\mathcal{K}_{\rm UV,1500}$ depends on the IMF of the stellar population, which remains uncertain at high redshift. Proposed high-redshift and Population III IMFs may shift the magnitude at which galaxies of a given mass enter the observable magnitudes of JWST. In particular, several studies propose that a top-heavy IMF may be present in high-redshift, Population III environments due to their low metallicity and/or high cosmic microwave background temperature (e.g., Omukai et al. 2005; Hirano et al. 2014, 2015; Chon et al. 2022). Such an IMF would lead to increased UV luminosity from nebular emission, increasing our $L_{\rm UV,1500}$ for a given $\dot{M}_*$. Thus, we adopt the standard value of $\mathcal{K}_{\rm UV,1500}$ both as a conservative estimate of detectability and for ease of comparison with other works. This work assumes that the stream velocity does not affect the high-redshift IMF, and further work is needed to ascertain whether such a dependence exists. Under this assumption, the shape of the UVLF should be consistent between the stream and nonstream velocity scenarios, although the overall height of both curves may vary given assumptions about $\mathcal{K}_{\rm UV,1500}$.

We must also correct our number counts for the fact that we have artificially increased σ_8 to 1.7 in order to gain more complete statistics when calculating number counts per volume in this study. We calculate a conversion factor from $\sigma_8 = 1.7$ to 0.8 as a function of mass using the Sheth & Tormen (2002) halo mass function (see Appendix A). In each magnitude bin,

we divide the number counts by the correction factor corresponding to the average mass in each bin. This introduces an additional uncertainty in the UVLF because of the range of halo masses represented at each magnitude.

3. Results

3.1. The Effect of Streaming on Star-forming Regions

As expected, the small-scale structure is suppressed in the presence of stream velocity (e.g., Tseliakhovich & Hirata 2010; Maio et al. 2011; Tseliakhovich et al. 2011; Fialkov et al. 2012; Naoz et al. 2012; O'Leary & McQuinn 2012; Bovy & Dvorkin 2013; Tanaka et al. 2013; Tanaka & Li 2014). Figure 1 shows an example of the projected density of a highly star-forming region with (left panels) and without (right panels) streaming. Both cases show the gas and star components separately (see labels). As depicted, small clumps of gas and stars in the $v_{\rm bc} = 0\sigma_{\rm bc}$ case are less apparent in the $v_{\rm bc} = 2\sigma_{\rm bc}$ case. Although Figure 1 shows just one example region, visual inspection of tens of highly star-forming objects in the simulation boxes reveals a similar pattern. We quantify the extent of these effects on star formation below, as they have implications for the SFR estimation and the luminosity of these objects.

3.2. Star Formation and the GSMF

Given that the stream velocity is expected to delay and suppress small-scale star formation at high redshift (e.g., Conaboy et al. 2023; Hegde & Furlanetto 2023; Schauer et al. 2023) and that JWST can already provide constraints on the low-mass end of the GSMF at redshifts as high as $z \sim 8$ (e.g., Navarro-Carrera et al. 2023), we calculate the GSMF in each simulation box to determine the expected contribution from the stream velocity.

The results are presented in Figure 2, where we show the GSMF in our simulation volume for the runs with (pink lines) and without (blue lines) the stream velocity. The two redshifts examined ($z = 12$ and 15) are displayed with solid and dashed lines, respectively. Above $M_* \gtrsim 10^{6.5} M_\odot$, the two curves agree. However, at lower masses, there are up to an order of magnitude more galaxies at each stellar mass in the run without the stream velocity.

The suppression in the GSMF in the $2\sigma_{\rm bc}$ run can be attributed to two effects caused by the stream velocity. First, the number density of all halos is suppressed in regions of streaming, leading to a suppression of the GSMF (see Figure 6 in Appendix A and, e.g., Naoz et al. 2013; Lake et al. 2021). Additionally, we show in Figure 3 the stellar mass as a function of halo mass for objects in each run. For a given stellar mass, the stars lie in a much larger halo in regions of streaming than without streaming. Thus, larger halos, which are less abundant according to the standard halo mass function, host galaxies of the same stellar mass for $M_* \lesssim 10^{6.5} M_\odot$, contributing fewer galaxies to the GSMF. As expected for a study with no feedback effects included, our simulated M_*/M_h at most masses is 10 or more times higher than is found by studies that include radiative and supernova feedback effects at similar redshift (e.g., Xu et al. 2016; Yeh et al. 2023). Typically, when feedback is included, $M_*/M_h \sim 10^{-3}$ (e.g., Garaldi et al. 2022; Yajima et al. 2023), while our study has objects mostly with $10^{-2} \lesssim M_*/M_h \lesssim 10^{-1}$.
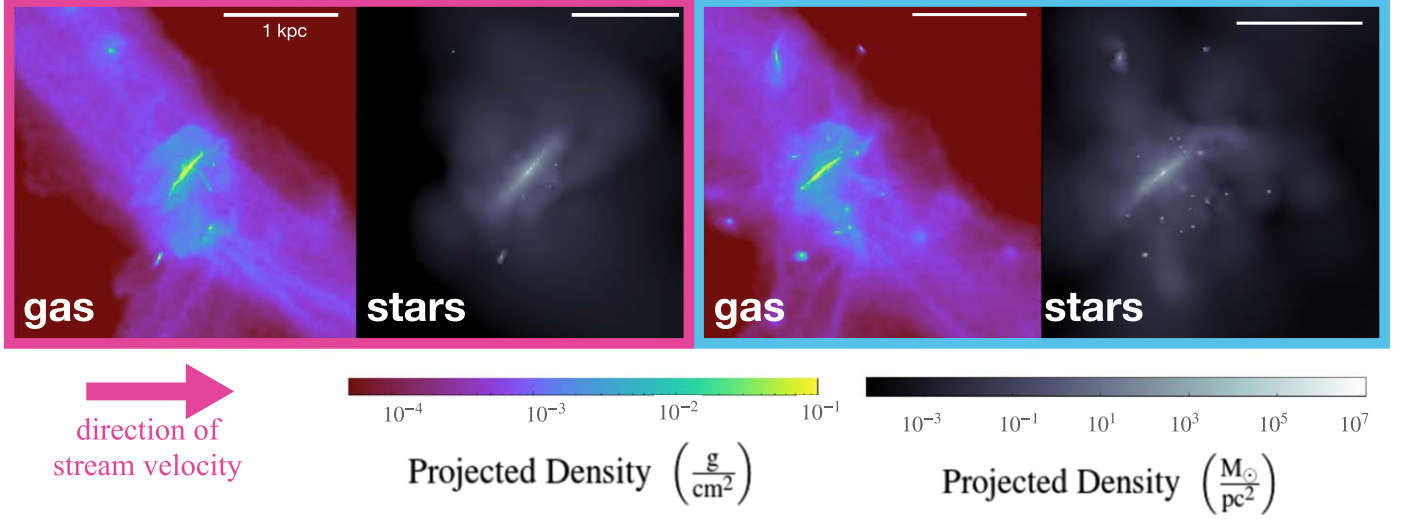
Figure 1. Comparison of the projected density of gas and stars in the region of a highly star-forming object in our simulations at $z = 12$ between the $2\sigma_{bc}$ run (left) and the $0\sigma_{bc}$ (right) run. A bar is shown in each panel denoting a distance of 1 kpc. Both the left and right boxes are centered on a galaxy in $2\sigma_{bc}$, and a physical offset of the location of the galaxy is noticeable as the $0\sigma_{bc}$ galaxy appears to the left of the box. This is due to the stream velocity, which points in the $+\hat{x}$ direction (to the right). The galaxy at the center of the left two panels formed stars rapidly between $z = 15$ and 12, with an SFR of $\dot{M}_* = 0.176\ M_\odot\ \mathrm{yr}^{-1}$, the fifth highest in our $2\sigma_{bc}$ run. It has $M_* = 10^{7.51}M_\odot$ at $z = 12$. The stellar mass history of this object in the interval between $z = 15$ and 12 is shown in Figure 7 in Appendix B.
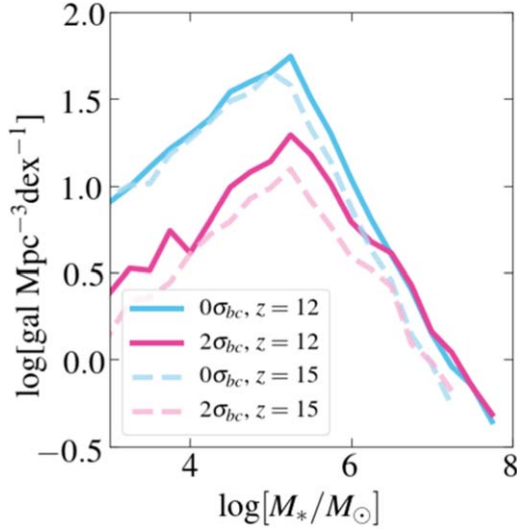

Figure 2. GSMF with (pink lines) and without (blue lines) stream velocity at $z = 12$ (solid) and 15 (dashed).

As demonstrated by Figure 3, while low stellar mass objects in the case with stream velocity have higher DM mass, the stream velocity and classical cases converge at large masses. Furthermore, the mass at which the two converge decreases with decreasing redshift. In other words, the blue ($0\sigma_{\mathrm{vbc}}$) and red ($2\sigma_{\mathrm{vbc}}$) points lie on top of each other for $M_* \geqslant 10^{7.0}M_\odot$ at $z = 15$. However, at $z = 12$, they converge at $M_* \geqslant 10^{7.25}M_\odot$, implying a fast SFR for the high masses with the stream velocity case between these two snapshots at $z = 15$ and 12.

This behavior is further illustrated in Figure 4, where the time evolution of the average stellar mass is shown for the most massive galaxies by stellar mass. As depicted, the SFR (the slope of the figure) in the stream velocity case is larger. Thus, although the star formation is suppressed for most galaxies in the stream velocity simulation run until $z \sim 15$, the SFR at large
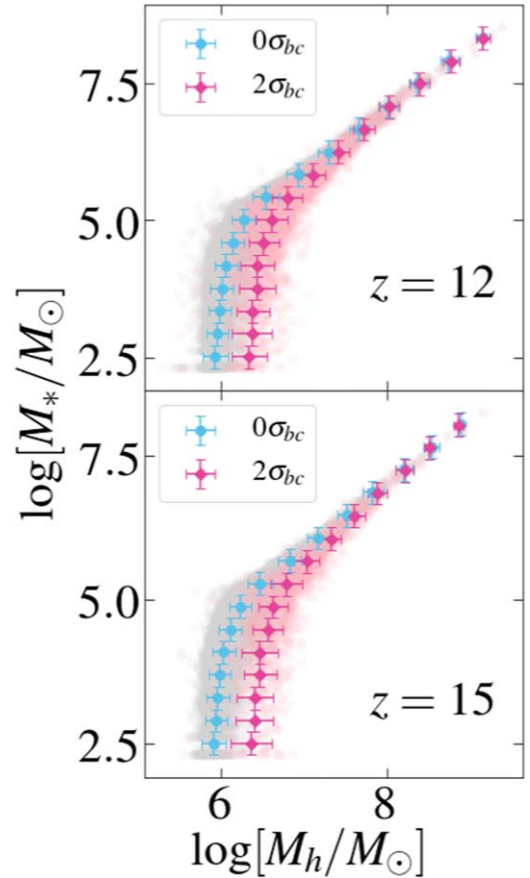

Figure 3. Stellar mass (M_*) vs. total halo mass (M_h) for the two runs at $z = 12$ (top) and 15 (bottom). The data are binned along the y-axis and shown with error bars corresponding to one standard deviation. The $0\sigma_{bc}$ run is given in blue (left points), and the $2\sigma_{bc}$ run is in pink (right points). Underneath the binned data, the actual distributions are shown, with the $0\sigma_{bc}$ runs shown in gray and the $2\sigma_{bc}$ runs shown in pink.
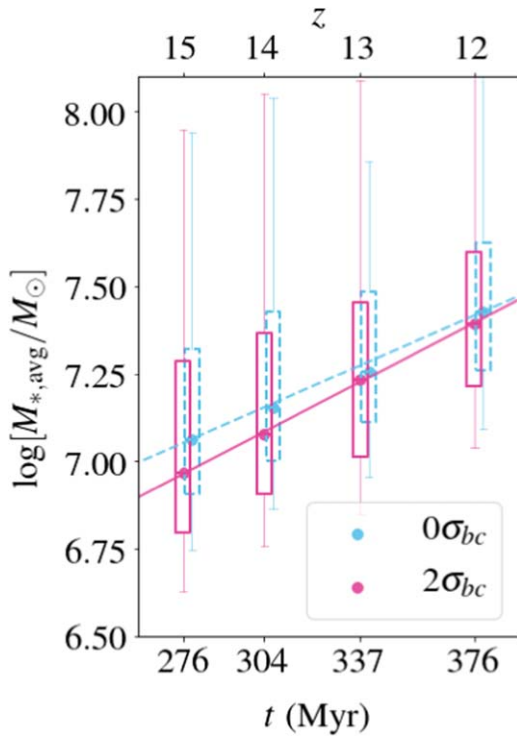
Figure 4. Box plot of stellar mass in the most massive 100 galaxies in the simulation between $z = 15$ and 12. The medians are shown as circles, and the boxes extend from the first to the third quartiles at each redshift. For clarity, the dashed blue boxes corresponding to the no stream velocity case have been offset along the x-axis by $+3$ Myr. Best-fit lines to the medians give $\log_{10}(M_*/M_\odot) = 0.0043 \log_{10}(t/\mathrm{Myr}) + 5.78$ for the stream velocity run (solid line) and $\log_{10}(M_*/M_\odot) = 0.0036 \log_{10}(t/\mathrm{Myr}) + 6.06$ for the no stream velocity run (dashed line). This panel highlights the difference between the large masses shown in Figure 3 as a function of redshift. Whiskers extend to the most distant data point within 1.5 times the interquartile range from the box.

masses with a large stream velocity is heightened between $z = 15$ and 12. Specifically, at $z = 12$, the mean SFR among galaxies with $M_* > 10^7 M_\odot$ that actively formed stars between $z = 13$ and 12 was around twice as high in the stream velocity run (0.986 $M_\odot \, \mathrm{yr}^{-1}$) as in the run without the stream velocity (0.453 $M_\odot \, \mathrm{yr}^{-1}$).

3.3. The UVLF

Given the above prediction that the SFR is higher in patches of the Universe with high stream velocity at the redshifts probed by our simulation, we expect that high-redshift dwarfs will be brighter in UV emission in those patches.

Thus, as a second probe of the population of dwarf galaxies resulting from a streaming scenario versus the classical scenario, we calculate the rest-frame absolute UV magnitude M_{UV} of our objects at $z = 12$. This is done based on the SFR according to the procedure described in Section 2.

In the bottom panel of Figure 5, we show the distribution of objects in our simulation box binned by M_{UV}. For objects fainter than $M_{\mathrm{UV}} \sim -12$, the UV magnitudes follow the same trend as the stellar masses, with the stream velocity function only one-sixth of the no streaming case. However, a turnover occurs above $M_{\mathrm{UV}} \sim -12$, and the stream velocity counts are enhanced by a factor of over an order of magnitude at $M_{\mathrm{UV}} \sim -14$.

We show the UVLF in regions with and without streaming in the top panel of Figure 5. The trend in the distributions is reflected in the UVLF at the bright end of our sample as a turnover where the UVLF in the $2\sigma_{\mathrm{bc}}$ region is greater than the no streaming function. The enhancement in the UVLF below $M_{\mathrm{UV}} \sim -12$ in the presence of the stream velocity can be counterintuitive given the suppression in star formation and number density caused by the stream velocity in most other contexts, including the GSMF. As evident in Figure 3, there is no underlying overabundance of more massive galaxies by stellar mass (which have higher SFR) due to the stream velocity; at these larger masses, there are roughly equal abundances in both simulation runs. Instead, several effects play a role in boosting the UV luminosity of these more massive galaxies. Importantly, the UV luminosity in our model is proportional to the SFR of galaxies via Equation (1). Here, we discuss how the stream velocity in this model leads to a boost in the SFR of dwarf galaxies with slightly higher stellar mass ($M_* \gtrsim 10^{6.5} M_\odot$).

First, in regions with highly supersonic streaming flow, the small-scale structure of gaseous clumps is washed away (as shown by, e.g., Tseliakhovich & Hirata 2010; Maio et al. 2011; Tseliakhovich et al. 2011; Fialkov et al. 2012; Naoz et al. 2012; O'Leary & McQuinn 2012; Bovy & Dvorkin 2013; Tanaka et al. 2013; Tanaka & Li 2014). An example of this suppression is evident in the small region of our simulation snapshot at $z = 12$ depicted in Figure 1, where at least 13 small gaseous clumps are present around the central galaxy in the $0\sigma_{\mathrm{bc}}$ run, while only five similar clumps are present in the 2σ run. Thus, star formation without the stream velocity can proceed in small minihalos of condensed gas, contributing to the behavior of the low-mass GSMF in Figure 2. Small clumps of star formation corresponding to these gaseous clumps are seen in the right panel of Figure 1. In regions with the stream velocity, however, the same overall cosmic density of gas is still present. Having been swept away from clumps that would allow it to form small clusters, the diffuse gas streams back onto larger halos thanks to their gravitational influence over the region as the stream velocity decays. Thus, star formation is concentrated in larger dwarf galaxies rather than smaller minihalos. This suppresses the extreme faint end of the UVLF while increasing the luminosity of the larger dwarfs, producing the trend in Figure 5.

Furthermore, previous studies such as Stacy et al. (2011), Greif et al. (2011), and Schauer et al. (2017b, 2023) found a delay in star formation in regions of streaming. Schauer et al. (2023) found that by $z = 8$, dwarf galaxies in their simulations with the stream velocity had reached roughly the same stellar mass as their counterparts in regions without streaming. For example, Figure 4 of that study depicts a dwarf galaxy that reaches $\sim 10^7 M_\odot$ by the end of the simulation and grows at a rate of $\sim 0.031 \, M_\odot \, \mathrm{yr}^{-1}$ between $z = 15$ and 12, while during the same period in the run with the stream velocity, it grows at $\sim 0.038 \, M_\odot \, \mathrm{yr}^{-1}$. The authors note a modest effect of higher SFRs in their streaming run overall prior to $z \approx 8$, at which point the difference in mass between the runs becomes mostly stochastic. If stream velocity–induced dwarfs indeed catch up to the stellar mass of the nonstreaming population by the epoch of reionization after a delay in the onset of star formation, then they undergo a period of faster SFR than the nonstreaming case.

The UVLF at $z = 12$, which roughly tracks the instantaneous SFR at the redshift of observation, would be catching these objects in a period where they experience enhanced star
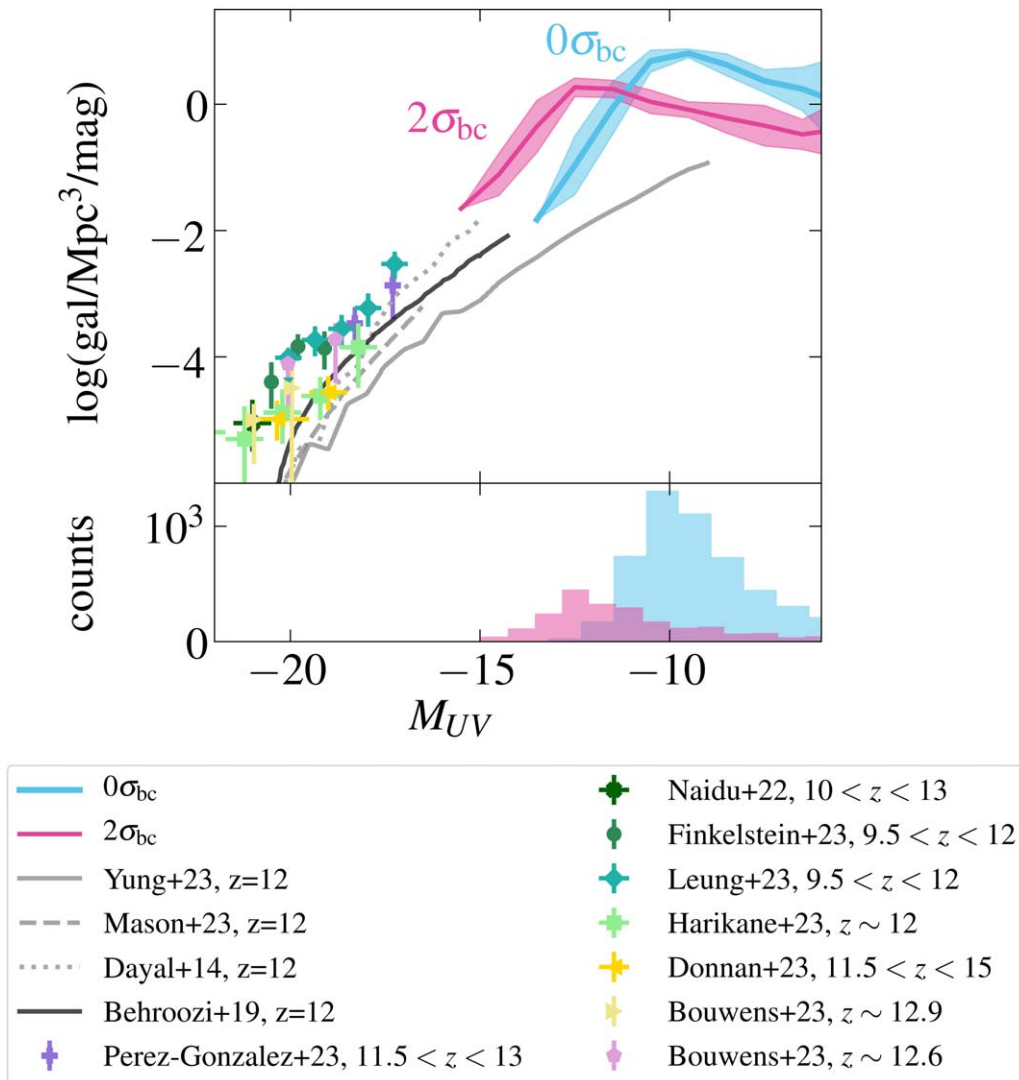
Figure 5. Top: UVLF at $z = 12$ with (pink) and without (blue) the stream velocity compared to the theoretical models of Yung et al. (2023), Mason et al. (2023), and Dayal et al. (2014) and observational constraints close to the redshift presented from Pérez-González et al. (2023), Naidu et al. (2022), Finkelstein et al. (2023), Leung et al. (2023), Harikane et al. (2023b), Donnan et al. (2023a), Bouwens et al. (2023), and Bouwens et al. (2023). The UVLF is then averaged over bins with $\Delta M_{UV} = 1$, with the shaded regions showing the minimum and maximum values in that box. Bottom: Distributions of galaxies by AB absolute UV magnitude with and without the stream velocity between $z = 13$ and 12.

formation thanks to the mechanism of concentrating gas into larger halos described above. We note that the baryonic feedback resulting from star formation episodes in these structures is not investigated here. Our UVLF can be understood as an upper limit in both cases given the likely reduction in star formation efficiency that would result from the inclusion of feedback in the simulation. A heightened SFR may lead to increased disruption due to feedback; however, as in Figure 3, dwarf galaxies with the stream velocity sit in larger DM halos in streaming cases, which may prevent disruption. The stream velocity may thus play a role in the "burstiness" of star formation at early times.

We overplot our results to several other theoretical models in the literature from Dayal et al. (2014), Behroozi et al. (2019), Yung et al. (2024), and Mason et al. (2023) at $z = 12$. Figure 5 thus demonstrates that the high-resolution investigation presented here allows us to reach the extremely faint end of the luminosity function. As this study does not include feedback effects, it is also relevant to note that our predicted $0\sigma_{bc}$ curves lie above the simulated UVLFs of radiation hydrodynamical

simulations in the literature that incorporate supernova and other feedback effects at similar redshift (e.g., Xu et al. 2016; Borrow et al. 2023), typically by around an order of magnitude. We note that none of these studies included the stream velocity effect.

In addition, we overplot some current observational JWST constraints. Our box size does not include enough objects bright enough to fall within the observable range of current JWST surveys. However, JWST studies focused on the faint end of the UVLF, such as Pérez-González et al. (2023) and Leung et al. (2023), are within a few magnitudes of our brightest galaxies. Given a strong lensing scenario, where magnifications allow for observations of objects that are an order of magnitude fainter than these studies, a measurement of the UVLF that reaches the predictions here may soon be possible.

4. Discussion and Conclusion

Our results imply that JWST observations of the faint end of the UVLF are close to a regime sensitive to the stream velocity. In particular, we predict that a high stream velocity patch will

contribute to a higher UVLF compared to the UVLF predicted by classic structure formation. This work also confirms that a strong suppression of galaxies with low stellar mass ($M_* \lesssim 10^{6.5} M_\odot$) is present in the early Universe due to the stream velocity.

Although this faint regime has not yet been detected, given that dwarf galaxies may contribute significantly to the production of ionizing photons at high redshift, the stream velocity effect may contribute to a spatial modulation in the progression of the early phases of reionization. Additionally, the suppression may persist to lower redshifts beyond the end of our simulation, where it could be detected by JWST or future missions that survey dwarf galaxies.

Our simulations do not include any baryonic feedback effects, and as expected, this increases our star formation efficiency in both runs by an order of magnitude in comparison to studies that include feedback effects. For example, both our stellar/halo mass function and our UVLF lie at least 10 times above the simulated halos of Xu et al. (2016), which include metal-free and metal-enriched star formation and feedback. Studies that investigated the stream velocity in the presence of feedback (e.g., Schauer et al. 2023) did not include a different prescription for feedback between the two cases and did not report a difference in the effects of feedback with and without the stream velocity. We caution that because feedback has some degenerate effects with a high stream velocity value, a boost or suppression in SFR of a single object is not enough to distinguish the stream velocity scenario. Instead, it will be necessary to investigate the overall population of objects, especially over large spatial scales. Given that the stream velocity coherence scale is on the order of a few tens of Mpc, observational measurements of the UVLF drawn from cosmic volumes much larger than the coherence scale will represent objects drawn from both low and high values of the stream velocity. Thus, the individual curves shown in our Figure 5 will not be resolved except by observations below the coherence scale. When comparing surveys selected from volumes larger than the coherence scale, the stream velocity effect should contribute to an overabundance of UV-bright galaxies, scattering points above the standard ΛCDM curve. Our results predict that observations from regions comparable to and smaller than the coherent length at a certain redshift would fall along a curve corresponding to a single value of the stream velocity. The stream velocity varies on spatial scales >a few Mpc and varies randomly in magnitude and direction in space following a Maxwell–Boltzmann distribution (e.g., Fialkov 2014). We note that this study only investigates the effects with a single value of the stream velocity as a proof of concept, and we leave detailed studies of intermediate or larger values to future work.

We suggest that as data sets at high redshift grow in completeness with future observations, it will be possible to undertake a statistical comparison of a larger cosmological volume to determine the presence of the stream velocity. Furthermore, since high-density peaks often correlate to large stream velocity values (e.g., Tseliakhovich et al. 2011), we expect that deep-field JWST observations will likely probe volumes formed in the presence of the stream velocity. For an ultradeep-field survey such as NGDEEP (e.g., Bagley et al. 2023), observing a highly magnified field ($\mu \sim 10$–50) that reaches $M_{UV} \sim -14$, we expect an enhanced luminosity function at the faint end.

JWST has opened a window into the high-redshift Universe and the earliest stages of galaxy formation, allowing for cosmological tests at earlier times than previously possible. While current interest often focuses on the observed discrepancies at the bright end of the UVLF, we propose that the faint end of the UVLF contains information about baryonic physics and the interaction with DM at early times. The stream velocity is a robust prediction of ΛCDM and is not present or decays rapidly in some alternative DM models (e.g., Nadler et al. 2019; Maamari et al. 2021; Driskell et al. 2022); thus, our methods represent a new test of ΛCDM structure formation and may help constrain alternative models. Such observed faint-end fluctuations in the UVLF on the coherence scale of the stream velocity would constitute the first high-redshift evidence of the presence of the stream velocity in the early Universe.

Appendix A
Clustering Correction Factor

In our simulations, the value of σ_8 is increased from the nominal value of $\sigma_8 = 0.8$ to 1.7 in order to increase the statistical power of our study without affecting the underlying cosmology. However, this results in an overabundance of halos. In order to describe the number density of objects in a typical region with $\sigma_8 = 0.8$, we apply an analytically calculated correction based on the Sheth & Tormen (2002) halo mass function. Following Naoz & Barkana (2007), we calculate the cumulative number density of halos,

$$n(>M_{\min}) = \int_0^\infty \frac{dn}{dM} dM, \qquad (A1)$$

using the Sheth & Tormen (2002) halo mass function with $\sigma_8 = 1.7$ and σ_8 at $z = 12$:

$$\frac{dn}{dM} = \frac{\rho_0}{M} f_{ST} \left| \frac{dS}{dM} \right|, \qquad (A2)$$

where

$$f_{ST}(\delta_c, S) = A' \frac{\nu}{S} \sqrt{\frac{a'}{2\pi}} \left[1 + \frac{1}{(a'\nu^2)^{q'}} \right] \exp\left(\frac{-a'\nu^2}{2} \right). \quad (A3)$$
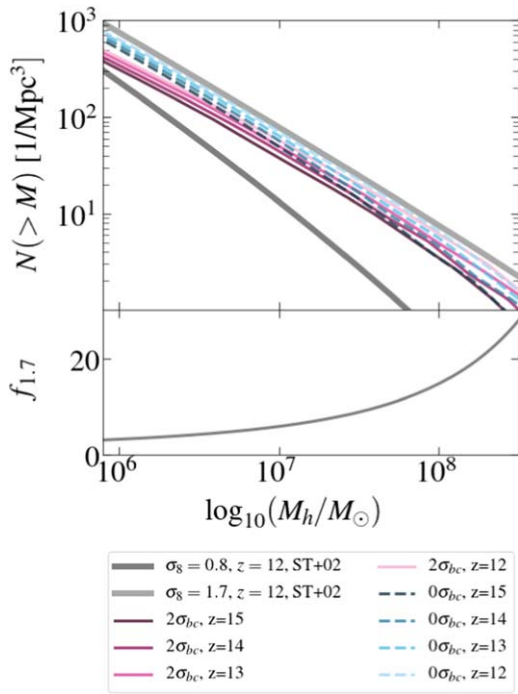
Figure 6. Top panel: the number of halos greater than mass M for the standard value $\sigma_8 = 0.8$ (dark gray) and 1.7 (light gray) used in the simulations presented here. The halo mass function from Sheth & Tormen (2002) is used. Also shown are the numerical results from our simulations at a selection of redshifts (pink and blue dashed lines). Bottom panel: the ratio between $n(>M)$ at $\sigma_8 = 0.8$ and 1.7 ($f_{1.7}$) as a function of halo mass. This ratio corresponds to the correction factor used to calibrate our UVLF.

Here, $\nu = \delta_c/\sqrt{S}$, $a' = 0.75$, $q' = 0.3$, $A' = 0.322$, and the critical collapse overdensity ($\delta_c(z)$) and the variance calculated from the power spectrum ($\sigma^2(M, z)$) are the arguments of Equation (A3) (Naoz & Barkana 2007, following Sheth & Tormen 2002). Our simulation number counts with $v_{bc} = 0\sigma_{vbc}$ are consistent with the Sheth & Tormen value (see top panel of Figure 6 comparing the numerical number counts to the analytical prediction). The correction factor is a function of mass. To correct the UVLF, we calculate the average mass in each bin and divide by the correction factor corresponding to the average mass. This introduces an uncertainty in our predicted value due to the range of masses in each magnitude bin. The correction factor is shown in the bottom panel of Figure 6.

Appendix B
Example Buildup of Stellar Mass

Figure 7 shows the stellar mass as a function of redshift for an example object in the simulation (thick dashed lines). In a period between $z = 15$ and 12, the object in the run with the stream velocity builds up the majority of its stellar mass, whereas its counterpart in the no stream velocity run does not undergo significant star formation because it already accrued the bulk of its stellar mass prior to that time. By $z = 12$, the object with the stream velocity has reached a similar mass to the object in the $0\sigma_{bc}$ run. In the background, similar tracks comparing objects with and without the stream velocity are shown in faint solid lines.
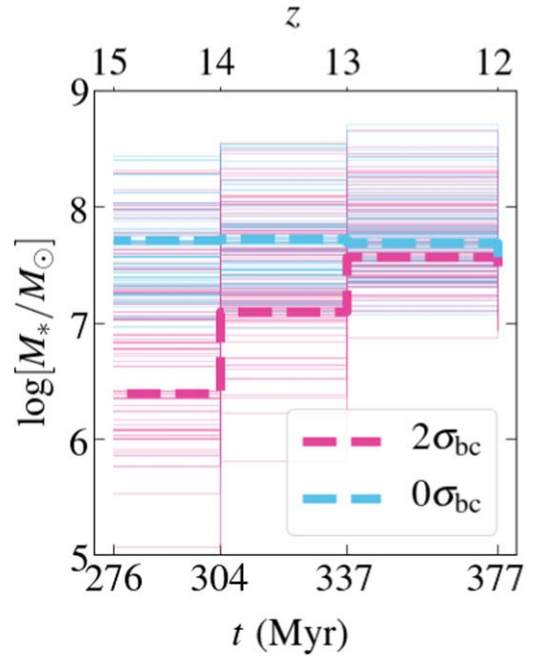

Figure 7. Stellar mass of massive objects between $z = 12$ and 15 with the stream velocity (pink) and the same object without the stream velocity (blue). An example object (the same object shown in the center of Figure 1) is shown in the thick dashed lines. In the simulation run with stream velocity (shown in pink), the object grows from $10^{6.39}$ to $10^{7.49} M_\odot$, whereas without the stream velocity (blue), the object has already formed the bulk of its stellar mass by that time.

ORCID iDs

Claire E. Williams ⓘ https://orcid.org/0000-0003-2369-2911
William Lake ⓘ https://orcid.org/0000-0002-4227-7919
Smadar Naoz ⓘ https://orcid.org/0000-0002-9802-9279
Blakesley Burkhart ⓘ https://orcid.org/0000-0001-5817-5944
Tommaso Treu ⓘ https://orcid.org/0000-0002-8460-0390
Federico Marinacci ⓘ https://orcid.org/0000-0003-3816-7028
Yurina Nakazato ⓘ https://orcid.org/0000-0002-0984-7713
Mark Vogelsberger ⓘ https://orcid.org/0000-0001-8593-7692
Naoki Yoshida ⓘ https://orcid.org/0000-0001-7925-238X
Gen Chiaki ⓘ https://orcid.org/0000-0001-6246-2866
Yeou S. Chiou ⓘ https://orcid.org/0000-0003-4962-5768
Avi Chen ⓘ https://orcid.org/0000-0002-8859-7790

References

Adams, N. J., Conselice, C. J., Ferreira, L., et al. 2023, MNRAS, 518, 4755
Arrabal Haro, P., Dickinson, M., Finkelstein, S. L., et al. 2023, ApJL, 951, L22
Asaba, S., Ichiki, K., & Tashiro, H. 2016, PhRvD, 93, 023518
Astropy Collaboration, Price-Whelan, A. M., Lim, P. L., et al. 2022, ApJ, 935, 167
Astropy Collaboration, Price-Whelan, A. M., Sipőcz, B. M., et al. 2018, AJ, 156, 123
Astropy Collaboration, Robitaille, T. P., Tollerud, E. J., et al. 2013, A&A, 558, A33
Atek, H., Shuntov, M., Furtak, L. J., et al. 2023, MNRAS, 519, 1201
Bagley, M. B., Pirzkal, N., Finkelstein, S. L., et al. 2023, arXiv:2302.05466
Behroozi, P., Wechsler, R. H., Hearin, A. P., & Conroy, C. 2019, MNRAS, 488, 3143
Borrow, J., Kannan, R., Garaldi, E., et al. 2023, MNRAS, 525, 5932
Bouwens, R., Illingworth, G., Oesch, P., et al. 2023, MNRAS, 523, 1009
Bouwens, R. J., Stefanon, M., Brammer, G., et al. 2023, MNRAS, 523, 1036
Bovy, J., & Dvorkin, C. 2013, ApJ, 768, 70
Bradley, L. D., Coe, D., Brammer, G., et al. 2023, ApJ, 955, 13
Bullock, J. S., & Boylan-Kolchin, M. 2017, ARA&A, 55, 343
Castellano, M., Fontana, A., Treu, T., et al. 2022, ApJL, 938, L15

Castellano, M., Fontana, A., Treu, T., et al. 2023, ApJL, 948, L14
Chiaki, G., & Wise, J. H. 2019, MNRAS, 482, 3933
Chiou, Y. S., Naoz, S., Burkhart, B., Marinacci, F., & Vogelsberger, M. 2019, ApJL, 878, L23
Chiou, Y. S., Naoz, S., Burkhart, B., Marinacci, F., & Vogelsberger, M. 2021, ApJ, 906, 25
Chiou, Y. S., Naoz, S., Marinacci, F., & Vogelsberger, M. 2018, MNRAS, 481, 3108
Chon, S., Ono, H., Omukai, K., & Schneider, R. 2022, MNRAS, 514, 4639
Conaboy, L., Iliev, I. T., Fialkov, A., Dixon, K. L., & Sullivan, D. 2023, MNRAS, 525, 5479
Dayal, P., Ferrara, A., Dunlop, J. S., & Pacucci, F. 2014, MNRAS, 445, 2545
Donnan, C. T., McLeod, D. J., Dunlop, J. S., et al. 2023a, MNRAS, 518, 6011
Donnan, C. T., McLeod, D. J., McLure, R. J., et al. 2023b, MNRAS, 520, 4554
Driskell, T., Nadler, E. O., Mirocha, J., et al. 2022, PhRvD, 106, 103525
Fialkov, A. 2014, IJMPD, 23, 1430017
Fialkov, A., Barkana, R., Tseliakhovich, D., & Hirata, C. M. 2012, MNRAS, 424, 1335
Finkelstein, S. L., Bagley, M. B., Arrabal Haro, P., et al. 2022, ApJL, 940, L55
Finkelstein, S. L., Bagley, M. B., Ferguson, H. C., et al. 2023, ApJL, 946, L13
Garaldi, E., Kannan, R., Smith, A., et al. 2022, MNRAS, 512, 4909
Greif, T. H., White, S. D. M., Klessen, R. S., & Springel, V. 2011, ApJ, 736, 147
Hagberg, A. A., Schult, D. A., & Swart, P. J. 2008, in Proc. 7th Python in Science Conf., ed. G. Varoquaux, T. Vaught, & J. Millman (Pasadena, CA: SciPy), 11
Harikane, Y., Nakajima, K., Ouchi, M., et al. 2024, ApJ, 960, 56
Harikane, Y., Ouchi, M., Oguri, M., et al. 2023, ApJS, 265, 5
Hegde, S., & Furlanetto, S. R. 2023, MNRAS, 525, 428
Hirano, S., Hosokawa, T., Yoshida, N., Omukai, K., & Yorke, H. W. 2015, MNRAS, 448, 568
Hirano, S., Hosokawa, T., Yoshida, N., et al. 2014, ApJ, 781, 60
Hirano, S., Shen, Y., Nishijima, S., Sakai, Y., & Umeda, H. 2023, MNRAS, 525, 5737
Hunter, J. D. 2007, CSE, 9, 90
Kennicutt, R. C., & Evans, N. J. 2012, ARA&A, 50, 531
Kennicutt, R. C., Jr. 1998, ARA&A, 36, 189
Lake, W., Naoz, S., Burkhart, B., et al. 2023a, ApJ, 943, 132
Lake, W., Naoz, S., Chiou, Y. S., et al. 2021, ApJ, 922, 86
Lake, W., Naoz, S., Marinacci, F., et al. 2023b, ApJL, 956, L7
Leung, G. C. K., Bagley, M. B., Finkelstein, S. L., et al. 2023, ApJL, 954, L46
Loeb, A., & Furlanetto, S. R. 2013, The First Galaxies in the Universe (Princeton, NJ: Princeton Univ. Press)
Maamari, K., Gluscevic, V., Boddy, K. K., Nadler, E. O., & Wechsler, R. H. 2021, ApJL, 907, L46
Madau, P., & Dickinson, M. 2014, ARA&A, 52, 415
Maio, U., Koopmans, L. V. E., & Ciardi, B. 2011, MNRAS, 412, 40
Mason, C. A., Trenti, M., & Treu, T. 2023, MNRAS, 521, 497
Morishita, T., & Stiavelli, M. 2023, ApJL, 946, L35
Nadler, E. O., Gluscevic, V., Boddy, K. K., & Wechsler, R. H. 2019, ApJL, 878, L32
Naidu, R. P., Oesch, P. A., van Dokkum, P., et al. 2022, ApJL, 940, L14
Nakazato, Y., Chiaki, G., Yoshida, N., et al. 2022, ApJL, 927, L12
Naoz, S., & Barkana, R. 2005, MNRAS, 362, 1047
Naoz, S., & Barkana, R. 2007, MNRAS, 377, 667
Naoz, S., Barkana, R., & Mesinger, A. 2009, MNRAS, 399, 369
Naoz, S., & Narayan, R. 2013, PhRvL, 111, 051303
Naoz, S., & Narayan, R. 2014, ApJL, 791, L8
Naoz, S., Yoshida, N., & Barkana, R. 2011, MNRAS, 416, 232
Naoz, S., Yoshida, N., & Gnedin, N. Y. 2012, ApJ, 747, 128
Naoz, S., Yoshida, N., & Gnedin, N. Y. 2013, ApJ, 763, 27
Navarro-Carrera, R., Rinaldi, P., Caputi, K. I., et al. 2023, arXiv:2305.16141
Nebrin, O., Giri, S. K., & Mellema, G. 2023, MNRAS, 524, 2290
Oke, J. B. 1974, ApJS, 27, 21
O'Leary, R. M., & McQuinn, M. 2012, ApJ, 760, 4
Omukai, K., Tsuribe, T., Schneider, R., & Ferrara, A. 2005, ApJ, 626, 627
Park, H., Ahn, K., Yoshida, N., & Hirano, S. 2020, ApJ, 900, 30
Pérez-González, P. G., Costantin, L., Langeroodi, D., et al. 2023, ApJL, 951, L1
Popa, C., Naoz, S., Marinacci, F., & Vogelsberger, M. 2016, MNRAS, 460, 1625
Roberts-Borsani, G., Treu, T., Chen, W., et al. 2023, Natur, 618, 480
Rohatgi, A., 2022 Webplotdigitizer: Version 4.6, https://automeris.io/WebPlotDigitizer
Sales, L. V., Wetzel, A., & Fattahi, A. 2022, NatAs, 6, 897
Schauer, A. T. P., Boylan-Kolchin, M., Colston, K., et al. 2023, ApJ, 950, 20
Schauer, A. T. P., Bromm, V., Boylan-Kolchin, M., Glover, S. C. O., & Klessen, R. S. 2021, ApJ, 922, 193
Schauer, A. T. P., Glover, S. C. O., & Klessen, R. S. 2017a, MmSAI, 88, 702
Schauer, A. T. P., Regan, J., Glover, S. C. O., & Klessen, R. S. 2017b, MNRAS, 471, 4878
Seljak, U., & Zaldarriaga, M. 1996, ApJ, 469, 437
Shen, X., Vogelsberger, M., Boylan-Kolchin, M., Tacchella, S., & Kannan, R. 2023, MNRAS, 525, 3254
Shen, X., Vogelsberger, M., Nelson, D., et al. 2020, MNRAS, 495, 4747
Sheth, R. K., & Tormen, G. 2002, MNRAS, 329, 61
Smith, B. D., Bryan, G. L., Glover, S. C. O., et al. 2017, MNRAS, 466, 2217
Springel, V. 2010, MNRAS, 401, 791
Stacy, A., Bromm, V., & Loeb, A. 2011, ApJL, 730, L1
Stark, D. P., Ellis, R. S., Bunker, A., et al. 2009, ApJ, 697, 1493
Sun, G., & Furlanetto, S. R. 2016, MNRAS, 460, 417
Tanaka, T. L., & Li, M. 2014, MNRAS, 439, 1092
Tanaka, T. L., Li, M., & Haiman, Z. 2013, MNRAS, 435, 3559
Tseliakhovich, D., Barkana, R., & Hirata, C. M. 2011, MNRAS, 418, 906
Tseliakhovich, D., & Hirata, C. 2010, PhRvD, 82, 083520
Turk, M. J., Smith, B. D., Oishi, J. S., et al. 2011, ApJS, 192, 9
Uysal, B., & Hartwig, T. 2023, MNRAS, 520, 3229
Vogelsberger, M., Marinacci, F., Torrey, P., & Puchwein, E. 2020a, NatRP, 2, 42
Vogelsberger, M., Nelson, D., Pillepich, A., et al. 2020b, MNRAS, 492, 5167
Williams, C. E., Naoz, S., Lake, W., et al. 2023, ApJ, 945, 6
Williams, H., Kelly, P. L., Chen, W., et al. 2023, Sci, 380, 416
Xu, H., Wise, J. H., Norman, M. L., Ahn, K., & O'Shea, B. W. 2016, ApJ, 833, 84
Yajima, H., Abe, M., Fukushima, H., et al. 2023, MNRAS, 525, 4832
Yan, H., Ma, Z., Ling, C., Cheng, C., & Huang, J.-S. 2023, ApJL, 942, L9
Yeh, J. Y. C., Smith, A., Kannan, R., et al. 2023, MNRAS, 520, 2757
Yung, L. Y. A., Somerville, R. S., Finkelstein, S. L., Wilkins, S. M., & Gardner, J. P. 2024, MNRAS, 527, 5929